Simultaneous measurement of temperature, stress, and electric field in GaN HEMTs with micro-Raman spectroscopy

Simultaneous measurement of temperature, stress, and electric field in GaN HEMTs with micro-Raman spectroscopy

Kevin R. Bagnall,[1] Elizabeth A. Moore,[2,3] Stefan C. Badescu,[2] Lenan Zhang,[1] and Evelyn N. Wang[1]
[1]*Department of Mechanical Engineering, Massachusetts Institute of Technology, Cambridge, Massachusetts 02139, USA*
[2]*Air Force Research Laboratory, Wright-Patterson AFB, Ohio 45433, USA*
[3]*KBRwyle, Dayton, Ohio 45431, USA*

(Received 4 May 2017; accepted 21 October 2017; published online 22 November 2017)

As semiconductor devices based on silicon reach their intrinsic material limits, compound semiconductors, such as gallium nitride (GaN), are gaining increasing interest for high performance, solid-state transistor applications. Unfortunately, higher voltage, current, and/or power levels in GaN high electron mobility transistors (HEMTs) often result in elevated device temperatures, degraded performance, and shorter lifetimes. Although micro-Raman spectroscopy has become one of the most popular techniques for measuring localized temperature rise in GaN HEMTs for reliability assessment, decoupling the effects of temperature, mechanical stress, and electric field on the optical phonon frequencies measured by micro-Raman spectroscopy is challenging. In this work, we demonstrate the simultaneous measurement of temperature rise, inverse piezoelectric stress, thermoelastic stress, and vertical electric field via micro-Raman spectroscopy from the shifts of the E_2 (high), A_1 longitudinal optical (LO), and E_2 (low) optical phonon frequencies in wurtzite GaN. We also validate experimentally that the pinched OFF state as the unpowered reference accurately measures the temperature rise by removing the effect of the vertical electric field on the Raman spectrum and that the vertical electric field is approximately the same whether the channel is open or closed. Our experimental results are in good quantitative agreement with a 3D electro-thermo-mechanical model of the HEMT we tested and indicate that the GaN buffer acts as a semi-insulating, p-type material due to the presence of deep acceptors in the lower half of the bandgap. This implementation of micro-Raman spectroscopy offers an exciting opportunity to simultaneously probe thermal, mechanical, and electrical phenomena in semiconductor devices under bias, providing unique insight into the complex physics that describes device behavior and reliability. Although GaN HEMTs have been specifically used in this study to demonstrate its viability, this technique is applicable to any solid-state material with a suitable Raman response and will likely enable new measurement capabilities in a wide variety of scientific and engineering applications. *Published by AIP Publishing.* https://doi.org/10.1063/1.5010225

I. INTRODUCTION

Gallium nitride (GaN) high electron mobility transistors (HEMTs) are a promising semiconductor technology for both high power radio frequency (RF) amplifier[1,2] and high voltage power conversion[3] applications, offering higher power density and efficiency than devices based on silicon (Si). However, the high power densities present in GaN HEMTs and their potential application in harsh environmental conditions lead to elevated channel temperatures. These elevated channel temperatures are believed to degrade device performance and accelerate device failures through thermoelastic (TE) stresses that induce structural damage in critical areas of the device.[4,5] It has also been suggested that electromechanical[4–6] and electrochemical[7] phenomena may induce structural and chemical changes to critical areas of these devices owing to the strong piezoelectricity of this material system and its susceptibility to the diffusion of moisture through the passivation layers. Although thermal and electro-thermo-mechanical modeling is a useful approach for understanding the temperature, stress, and electric field distributions in GaN HEMTs, the variation of material properties among different GaN epitaxial structures and the complex physics in these devices require experimental validation to ensure that modeling predictions are quantitatively accurate.

Due to its superior spatial resolution of ≈1 μm compared to ≈5 μm for infrared (IR) thermometry, micro-Raman thermometry is one of the most popular techniques for measuring local temperature rise in GaN HEMTs.[8–10] While the earliest reports of micro-Raman thermometry equated the shift in the Stokes peak positions with the temperature rise alone, subsequent studies have highlighted the importance of accounting for inverse piezoelectric (IPE)[11] and thermoelastic stresses[12] and have demonstrated the ability to simultaneously measure the temperature rise and thermoelastic stress in the ON state.[13,14] Yet, for several years, significant discrepancies have existed in the sign and order of magnitude of the IPE stress predicted by electro-mechanical modeling and measured by micro-Raman spectroscopy using the phonon stress coefficients.[11,15,16] In a recent study, we proposed that the vertical electric field along the *c*-axis strongly affects the Stokes peak positions of wurtzite GaN independently

of the IPE strain and needs to be accounted for with a term depending on the electric field apart from that of the stress in the *c*-plane.[17] We also validated our hypothesis with measurements of the vertical electric field and in-plane IPE stress in GaN HEMTs using the simultaneous change in the Stokes peak position of two phonon modes.

In this work, we demonstrate the simultaneous measurement of temperature rise, in-plane stress, and the vertical electric field in GaN HEMTs using the simultaneous change in the position of three phonon modes, i.e., E_2 (high), A_1 longitudinal optical (LO), and E_2 (low), at any arbitrary gate and drain bias. This technique overcomes the limitation of previous approaches that measure temperature rise in GaN HEMTs in the ON state by using the pinched OFF state as the unpowered reference and assuming that the pinched OFF state removes the effects of IPE stress on the Raman spectrum. We show that micro-Raman measurements in the pinched OFF state with the three-peak fit method exhibit the same vertical electric field and in-plane stress validated in our previous work with two peaks[17] yet with zero temperature rise. Measurements in the ON state using our three-peak fit method yield the same vertical electric field as in the pinched OFF state at the same drain bias and approximately the same temperature rise and in-plane stress as the two-peak fit method with the pinched OFF state as the unpowered reference.[13,14] Our measurements show good, quantitative agreement with our electro-thermo-mechanical model presented in this work and provide helpful physical insights into the electrostatic behavior of the GaN buffer. In addition to presenting a clear and systematic explanation of the Raman peak position changes observed in GaN HEMTs due to thermal, mechanical, and electrical changes, our work suggests that the same methodology can be applied to a variety of semiconductor devices to probe complex electro-thermo-mechanical phenomena and validate multiphysics models.

Apart from its specific application to GaN HEMTs, our Raman-based simultaneous stress, electric field, and temperature measurement technique is one of the only a limited number of optical techniques available to measure electric fields in semiconductor devices. Other such techniques are based on the Kerr effect,[18] Pockels effect,[19] Franz-Keyldish oscillations excited by photoreflectance,[20] and optically detected magnetic resonance in nitrogen-vacancies in diamond.[21] However, each of these techniques has disadvantages, such as large uncertainty and poor spatial resolution[18] or the necessity of above bandgap optical excitation,[20] which generates excess carriers. In contrast, the Raman-based technique presented in this work offers high spatial resolution, good sensitivity, and relative simplicity of the experimental setup in view of the wide availability of commercial micro-Raman systems. Also, we believe our technique to be one of the only such optical electrometry techniques capable of decoupling the electric field from the stress and temperature in semiconductor devices at an arbitrary bias condition. However, it is limited to crystal classes for which one or more of the electric field components induce a first-order shift in the phonon frequencies.

Section II explains the theory of micro-Raman thermometry in GaN HEMTs, the various approaches to extracting the temperature rise from Raman spectra, and the simultaneous temperature, stress, and electric field measurement technique developed in this work. Section III describes our micro-Raman spectroscopy setup and the measured changes in Raman peak positions in the pinched OFF state and ON state of the GaN HEMT we tested. Section IV introduces the 2D semiconductor and 3D electro-thermo-mechanical modeling framework that supports our experimental results. Section V provides an analysis of the experimental and modeling results, showing good agreement between the model and experiment and highlighting the physical insights gained from our measurements. Finally, Sec. VI concludes with the key results of our work. We anticipate that this implementation of micro-Raman spectroscopy with the proper interpretation of the experimental data will be very valuable in future efforts to accurately measure the local temperature rise and develop a holistic picture of semiconductor device reliability in terms of the coupled electro-thermo-mechanical physics of failure.

II. THEORY

A. Phonon frequency response to temperature, stress, and electric field

Micro-Raman spectroscopy is one of the most common techniques for characterizing the properties of III-nitride materials due to the strong Raman activity of these materials, the relative simplicity of the experimental setup, and the wide availability of commercial micro-Raman systems.[22] In the Raman scattering process, a photon of wavelength λ_0 from the excitation source (typically a narrow linewidth laser) scatters inelastically to a different wavelength λ by emitting (Stokes process) or absorbing (anti-Stokes process) an optical phonon in the sample. Each optical phonon mode that is allowed by Raman scattering selection rules appears as a peak with a centroid ω and linewidth Γ that are related to the phonon frequency and lifetime. The Raman peak position $\omega = \lambda_0^{-1} - \lambda^{-1}$ specified in units of cm^{-1} is proportional to the phonon frequency, and the linewidth Γ (apart from the peak broadening introduced by the spectrometer) is inversely proportional to the phonon lifetime through the Heisenberg uncertainty relation.[23] Due to the fact that the phonon frequencies, lifetimes, and populations all vary with temperature, the Stokes peak positions, Stokes peak linewidths, and/or Stokes/anti-Stokes intensity ratio may be used to measure the temperature in GaN HEMTs with micro-Raman spectroscopy.[9,12,14] For wurtzite GaN, Ga-face HEMTs with the laser excitation incident along $[000\bar{1}]$, and the Raman scattered light collected along [0001], i.e., the $\bar{z}(-,-)z$ backscattering configuration, only the E_2 (high), A_1 (LO), and E_2 (low) phonon modes are allowed[10] as shown in Fig. 1.

The earliest studies of micro-Raman thermometry in GaN HEMTs[8,9] utilized an empirical, nonlinear expression for the temperature dependence of the E_2 (high) peak position,

$$\omega(T) = \omega(T=0) - \frac{C}{e^{D\cdot hc\omega(T=0)/k_B T} - 1}, \tag{1}$$

where $\omega(T)$ is the Raman peak position at the temperature T in kelvin, $\omega(T=0)$ is the Raman peak position at absolute zero

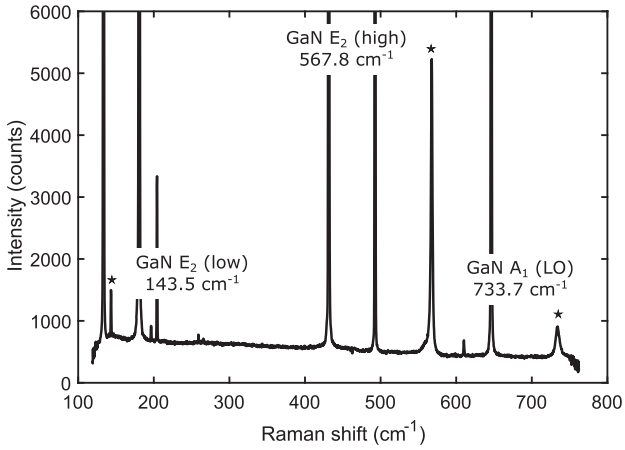

FIG. 1. Example Raman spectrum of wurtzite GaN with 632.9 nm excitation taken with the experimental setup described in Sec. III. The GaN E_2 (high), A_1 (LO), and E_2 (low) peaks with their frequencies are indicated by the stars. The other peaks are the Raman peaks of the 4H–SiC substrate or spontaneous emission lines from the neon lamp used for calibration.

temperature, and C and D are empirical constants determined by calibration.[24] Owing to the fact that different GaN epilayers grown on various foreign substrates and bulk GaN grown by different methods have a different amount of residual stress and different induced thermoelastic stress levels as the temperature changes, each GaN sample has different values of the constants $\omega(T=0)$, C, and D. Later, Choi *et al.*[14] demonstrated a methodology for resolving these issues and eliminating the need to calibrate each sample with linear terms that depend on temperature and stress,

$$[\omega_{ON} - \omega_{OFF}]_n \approx \frac{1}{2}K_n\left(\sigma_{xx} + \sigma_{yy}\right)^{TE} + A_n\Delta T, \qquad (2)$$

where ω_{ON} and ω_{OFF} are the Raman peak position of the nth phonon mode measured in the ON state and the pinched OFF state at the same drain bias, A is the temperature coefficient, $\Delta T = T - T_0$ is the temperature rise, K is the biaxial stress coefficient, and $(\sigma_{xx} + \sigma_{yy})^{TE}/2$ is the average stress in the c-plane, herein referred to as the "in-plane stress," induced by the thermoelastic (TE) effect. Provided that the coefficients A and K are known for the E_2 (high) and A_1 (LO) modes, Eq. (2) written for each of these peaks can be used to self-consistently measure the temperature rise and thermoelastic stress from the change in the Raman peak position of these two modes. Although it is widely believed that using the pinched OFF state peak position ω_{OFF} as the unpowered reference in both Eqs. (1) and (2) removes the effect of the IPE stress on the Raman peak positions, analyzing Raman peak position changes between the pinched OFF state and the zero bias state ω_0 ($V_{ds} = 0$) with the linear stress coefficient formula $\omega_{OFF} - \omega_0 = \frac{1}{2}K\left(\sigma_{xx} + \sigma_{yy}\right)^{IPE}$ results in measured IPE stress values that are one order of magnitude larger than modeled values and with opposite signs for the E_2 (high) and A_1 (LO) modes.[11,16]

In our recent study exploring the electric field dependence of the Raman peaks of wurtzite GaN,[17] we showed that fundamentally the optical phonon modes with E_2 and A_1 symmetry in wurtzite crystals shift linearly with temperature, stress, and electric field according to

$$\Delta\omega_{E_2} = \frac{1}{2}K_{E_2}\left(\sigma_{xx} + \sigma_{yy}\right) + \tilde{b}_{E_2}\sigma_{zz} \pm \tilde{c}_{E_2}\sqrt{\left(\sigma_{xx} - \sigma_{yy}\right)^2 + 4\sigma_{xy}^2} + B_{E_2}E_z + A_{E_2}\Delta T, \qquad (3)$$

$$\Delta\omega_{A_1} = \frac{1}{2}K_{A_1}\left(\sigma_{xx} + \sigma_{yy}\right) + \tilde{b}_{A_1}\sigma_{zz} + B_{A_1}E_z + A_{A_1}\Delta T, \qquad (4)$$

where $\Delta\omega$ is the shift in the Raman peak position between two states, K and A are the same biaxial stress and temperature coefficients as in Eq. (2), $\tilde{b}$ is the phonon stress coefficient along the c-axis, $\tilde{c}$ is the phonon shear stress coefficient in the c-plane, and B is the electric field shift coefficient. The numerical values of these coefficients are different for each of the optical phonon modes, including the E_2 (high) and E_2 (low) modes despite these modes both transforming as E_2. While the relations in Eqs. (2)–(4) are linear approximations of the generally nonlinear dependence of the Raman peak position on temperature, stress, and electric field, Choi *et al.* verified their linear behavior from 25 °C to 300 °C and ±1 GPa for the temperature and stress,[14] and our previous density functional theory (DFT) calculations indicate that the shift with vertical electric field is linear for ±5 MV/cm,[17] which are typical operating conditions for GaN HEMTs.

Equations (3) and (4) together with Fig. 2 showing the output ($I_d - V_{ds}$) characteristics of a GaN HEMT can be used to explain which of the physical quantities (temperature rise, IPE stress, thermoelastic stress, total induced stress, and vertical electric field) are measured by the change in peak position $\Delta\omega$ between any two bias points. In general, the asymmetry of the stress in the c-plane $|\sigma_{xx} - \sigma_{yy}|$ and the shear stress σ_{xy} are small compared to the average stress in the c-plane $(\sigma_{xx}+\sigma_{yy})/2$ so that the third term in Eq. (3) may be neglected. There is typically no mechanical force constraining the movement of the top surface of the HEMT so the stress along the c-axis σ_{zz} is also much smaller than the stress in the

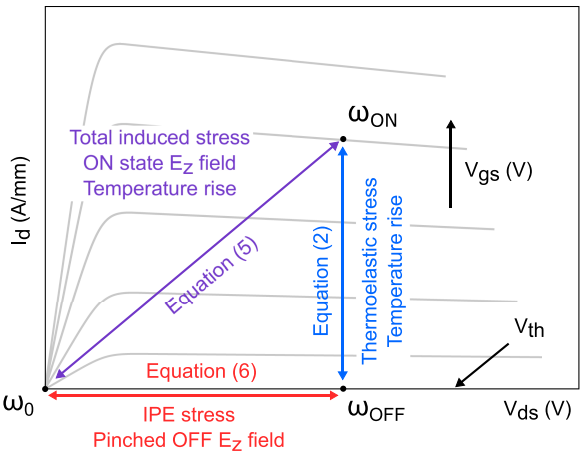

FIG. 2. Output drain current-drain voltage ($I_d - V_{ds}$) characteristics showing the contributions of the temperature rise, stress, and electric field in the ON state and pinched OFF state to the shift in the Raman peak positions according to Eqs. (2), (5), and (6). One should note that the thermoelastic stress, IPE stress, and total induced stress described by this figure are stresses induced by changing the gate and drain bias.

c-plane, and the second term in Eqs. (3) and (4) may also be neglected. Then, the change in the Raman peak position between any bias point in the ON state ($V_{ds} \geq 0$ and $V_{gs} > V_{th}$, where V_{th} is the gate threshold voltage) and zero drain bias is given by

$$[\omega_{ON}(V_{ds} \geq 0) - \omega_0(V_{ds} = 0)]_n \approx \frac{1}{2} K_n \left(\sigma_{xx} + \sigma_{yy}\right) + B_n E_z^{ON} + A_n \Delta T. \quad (5)$$

This general expression we have written for the ON state also applies for the pinched OFF state at $V_{ds} \geq 0$ and $V_{gs} < V_{th}$ but can be further simplified to

$$[\omega_{OFF}(V_{ds} \geq 0) - \omega_0(V_{ds} = 0)]_n \approx \frac{1}{2} K_n \left(\sigma_{xx} + \sigma_{yy}\right)^{IPE} + B_n E_z^{OFF} \quad (6)$$

because we expect the temperature rise to be negligible due to the very low dissipated power when $V_{gs} < V_{th}$. In Eq. (6), we have also added a superscript of "IPE" to indicate that the average in-plane stress is only associated with the IPE effect; the thermoelastic stress is negligible when the temperature rise is negligible. Finally, assuming that the total induced stress is the sum of the IPE and thermoelastic stresses $\sigma_{ij} = \sigma_{ij}^{IPE} + \sigma_{ij}^{TE}$ and that the vertical electric field in the GaN buffer primarily depends on the drain bias, i.e., $E_z^{OFF} \approx E_z^{ON}$, Eq. (6) can be subtracted from Eq. (5) to yield Eq. (2) introduced by Choi *et al.*[14] One should note that the phonon frequency shifts associated with the TE stress, the IPE stress, and the total induced stress occur when the device bias is changed; they are separate from the residual stress in the GaN buffer that occurs during epitaxial growth on a foreign substrate. The residual stress/strain in the buffer associated with the epitaxial growth process is accounted for by the shift between the zero bias frequency ω_0 in Fig. 2 and the frequency of theoretically strain-free wurtzite GaN [e.g., 568.15 cm^{-1} and 733.94 cm^{-1} for the E_2 (high) and A_1 (LO) modes[25]].

Equation (5) provides the theoretical basis for the simultaneous measurement of temperature, stress, and electric field via micro-Raman spectroscopy proposed in this work. If one could measure the Raman peak position changes for three phonon modes, then the total induced in-plane stress (the sum of the IPE and thermoelastic stresses), the ON state vertical electric field, and the temperature rise could be simultaneously measured using Eq. (5). If only two Raman peaks are available, then Eq. (6) can be used to measure the IPE stress and the vertical electric field in the pinched OFF state or Eq. (2) can be utilized to measure the temperature rise and thermoelastic stress in the ON state (with the pinched OFF state as the unpowered reference). Whether Eq. (5) is used with three peaks or Eq. (2) is used with two peaks, the measured temperature rise ΔT should be the same. Measurements of the vertical electric field E_z in the ON state and the pinched OFF state using Eqs. (5) and (6) should also yield approximately the same value of E_z if indeed E_z in the buffer primarily depends on the drain bias.[11,16,17]

B. Phonon frequency shift coefficients

Simultaneous measurement of the temperature, stress, and electric field using Eq. (5) and the measured frequency shifts of the E_2 (high), A_1 (LO), and E_2 (low) modes require accurate values of the coefficients K, A, and B for all three modes. In Table I, we list the measured and calculated values of these coefficients from the literature and this work. The biaxial stress coefficients K of the E_2 (high) and A_1 (LO) modes have been measured directly[25] or indirectly[26] by multiple groups with similar values, suggesting that these values are known to be within 10% accuracy or better. The temperature coefficients A of the E_2 (high) and A_1 (LO) modes were measured by Choi *et al.*[14] in a bulk GaN HVPE sample, which we believe to also be similarly accurate. Bagnall *et al.*[17] reported the electric field coefficient B for all three modes calculated by DFT, but the lower vertical electric field measured in the pinched OFF state with the E_2 (high) and E_2 (low) modes compared to the E_2 (high) and A_1 (LO) modes suggests that perhaps the actual $B_{E_2(\ell)}$ coefficient is smaller than the value of –0.47 cm^{-1}/(MV/cm) calculated in that work. Due to the limited data available in the literature for the E_2 (low) mode, we calculated new values of the stress and electric field coefficients and measured the temperature and stress coefficients of the E_2 (low) mode in this work.

The first principles calculations were performed within the Perdew-Zunger local density approximation (PZ-LDA) of DFT implemented in the QUANTUM ESPRESSO code.[27]

TABLE I. Biaxial stress, temperature, and electric field coefficients for the zone center optical phonon modes of wurtzite GaN observed in the backscattering $\bar{z}(-,-)z$ configuration with Raman spectroscopy. The values in square brackets are those used in the analysis of the experimental data in Sec. V.

	K (cm^{-1}/GPa)	A (cm^{-1}/K)	B [cm^{-1}/(MV/cm)]
E_2 (high)	−3.27 ± 0.15[a] [−3.20[b]]	−0.015 ± 0.0001[d] [−0.0138 ± 0.0001[e]]	−1.38[f] [−1.36[b]]
A_1 (LO)	−2.21 ± 0.10[a] [−2.21[b]]	−0.0281 ± 0.0001[d] [−0.0263 ± 0.0001[e]]	2.05[f] [2.09[b]]
E_2 (low)	0.28 ± 0.01[c] [0.28[b]]	[−0.0034 ± 0.0001[e]]	−0.47[f] [−0.26[b]]

[a]Experimental value[25] adjusted with the elastic constants from Ref. 30. The values in Table I are revised values, which are slightly different from the values previously reported in Ref. 17.
[b]*Ab initio* (DFT) calculation, this work and Ref. 33.
[c]Experimental value, this work and Ref. 33.
[d]Experimental value measured from 25 °C to 300 °C.[14]
[e]Experimental value measured from 20 °C to 200 °C, this work.
[f]*Ab initio* (DFT) calculation[17] combined with the experimental strain phonon deformation potentials (PDPs) from Refs. 25–34 and experimental piezoelectric moduli from Ref. 30.

We used projector-augmented wave (PAW) pseudopotentials with plane-wave cutoffs of 60 Ry and 240 Ry for the energy and electronic density, respectively, and a 12 × 12 × 6 Brillouin zone sampling grid. The phonon spectra were calculated using a single unit cell within the density functional perturbation theory (DFPT) formalism.[28] We found this choice of density functional and pseudopotentials to give good agreement with experimental values of the lattice parameters,[29] elastic constants,[30] and phonon frequencies.[31] The strain phonon deformation potentials (PDPs) entering into the biaxial stress coefficients K were calculated from seven equally spaced strain values ϵ_{ii} from −0.012 to 0.012. For the electric field coefficients B, we used the QUANTUM ESPRESSO implementation of the modern theory of polarization, taking seven equally spaced electric field values in the range from −9 MV/cm to 9 MV/cm.[32] Further details on these first principles calculations will be published in the future.[33]

The values of the stress and electric field coefficients of the E_2 (high) and A_1 (LO) modes calculated by this methodology and listed in Table I agree to be within 5% of the values of K measured by Choi *et al.*[14] and B calculated by Bagnall *et al.*[17] via DFT in a different software package. The stress coefficient of the E_2 (low) mode calculated in this work (0.28 cm^{-1}/GPa), however, differs significantly from that of $K_{E_2(\ell)} = 1.09 \pm 0.11$ cm^{-1}/GPa derived from independent measurements of the stress coefficient along the c-axis $\tilde{b}_{E_2(\ell)} = 0.79 \pm 0.04$ cm^{-1}/GPa[26] and hydrostatic pressure coefficient $K_{E_2(\ell)} + \tilde{b}_{E_2(\ell)} = 0.3 \pm 0.1$ cm^{-1}/GPa.[34] To validate our calculated value of $K_{E_2(\ell)}$, we also measured this stress coefficient from the residual stress in GaN epilayers on 4H–SiC and sapphire substrates and obtained a value in very good agreement with the calculated value (0.28 ± 0.01 cm^{-1}/GPa).[33] Although we do not know the reason for the discrepancy between the value calculated and measured in this work and that reported in a previous study,[26] we believe that the value of $K_{E_2(\ell)} = 0.28$ cm^{-1}/GPa is accurate. Due to the fact that Choi *et al.*[14] did not report a value for the temperature coefficient of the E_2 (low) mode, we measured $A_{E_2(\ell)}$ in this work using the experimental setup described in Sec. III. Our calculated electric field coefficients agreed to be within 5% of the values reported by Bagnall *et al.*[17] for the E_2 (high) and A_1 (LO) modes but yielded a smaller value of $B_{E_2(\ell)} = -0.26$ cm^{-1}/(MV/cm).

III. EXPERIMENTAL SETUP AND MEASUREMENTS

Similar to our previous work,[17] we measured changes in the Raman peak positions of commercially available, discrete GaN HEMTs fabricated on 4H-SiC substrates (CGHV1J006D, Cree) designed for RF applications. The GaN HEMT was mounted to the 5 × 5 mm^2 quad flat no leads (QFN) milled-out package (Open-Pak, SEMPAC) with ≈50 μm thick silver (Ag)-filled epoxy (Duralco 120, Cotronics), which was soldered to a printed circuit board (PCB), mounted on a 3 mm thick copper block, and maintained at a constant base temperature by a thermoelectric cooler (TEC, TE-127-1.0-2.5, TE Technology). The epitaxial structure of these 6 × 200 μm HEMTs as reported by the manufacturer include an ≈20 nm $Al_{0.22}Ga_{0.78}N$ barrier, ≈1 nm thick AlN interlayer, 1.4 μm iron (Fe)-doped GaN buffer, and 100 μm 4H–SiC substrate with a gate length of $L_g = 0.25$ μm.[35] Cross-sectional scanning electron microscopy (SEM) images also show the presence of an ≈50 nm thick AlN nucleation layer between the GaN buffer and SiC substrate, a gate-connected field plate, and a source-connected field plate (SCFP).

Raman spectra of the GaN buffer were collected in the $\bar{z}(-,-)z$ backscattering configuration with the free space micro-Raman spectroscopy system described in our previous work[17] and shown in Fig. 3. The system consists of a single longitudinal mode diode laser (λ = 632.904 nm, SLM-FS, REO), an optical microscope (BX41, Olympus), a dichroic beam splitter (LPD02-633RU-25, Semrock) and a long pass

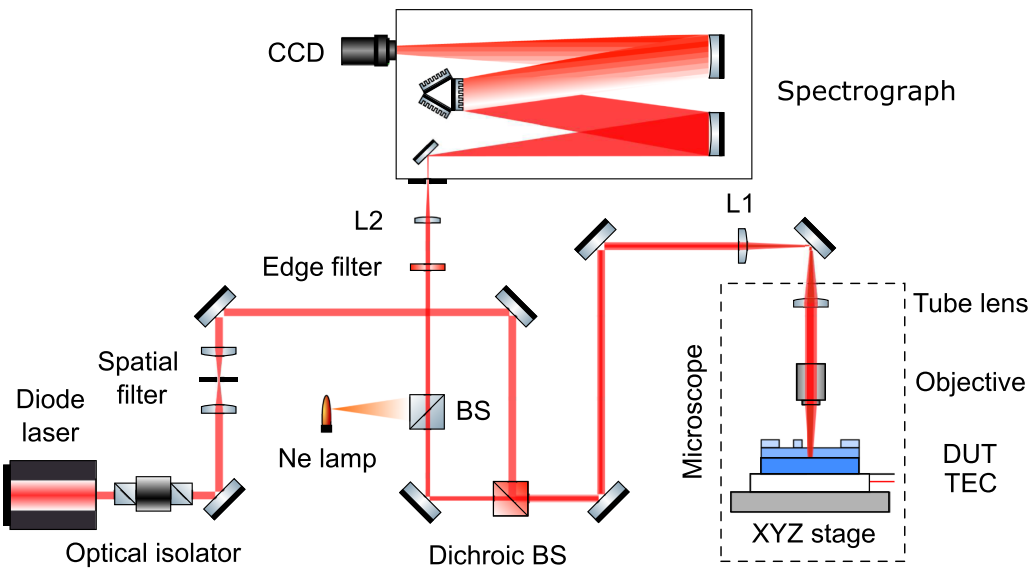

FIG. 3. Micro-Raman spectroscopy system developed for this work. "BS" and "L" refer to beam splitter and lens, respectively.

edge filter (LP02-633RU-25, Semrock), and a 750 mm focal length spectrograph (Acton Spectra-Pro SP-2750, Princeton Instruments) equipped with a 1800 G/mm grating. The 100×, *NA* = 0.8 microscope objective (LMPlanFL N, Olympus) used to focus the laser excitation on the sample and collect the Raman scattered light resulted in a laser spot size of ≈1.0 μm and a depth of field of ≈4 μm. The depth of field being greater than the thickness of the GaN buffer (1.4 μm in our sample) indicates that the measured changes in the Raman peak positions represent the average through the thickness of the GaN buffer. The laser power measured at the sample plane was ≈20 mW, and the Raman collection time was 1 s. Each Raman peak was individually calibrated with the spontaneous emission lines of a neon calibration lamp (6032, Newport) placed in the optical path to ensure high precision and repeatability. For the measurement of the temperature coefficients listed in Table I, the change in Raman peak positions with increasing temperature from 20 °C to 200 °C was measured in a semi-insulating bulk GaN HVPE sample (GB.SE.010.Ga.C, Kyma Technologies) on a temperature stage with an accuracy of 0.5 °C (HCP621V, Instec).

The micro-Raman spectroscopy system was integrated with a precision source/measure unit (SMU, B2902A, Agilent) to simultaneously bias the HEMT or the device under test (DUT) and record Raman spectra while maintaining the backside temperature of the DUT at 20.0 ± 0.1 °C with the TEC. In order to illustrate the methodology of simultaneously measuring temperature, stress, and electric field shown in Fig. 2, we measured the shift in the Raman (Stokes) peak positions of the E_2 (high), A_1 (LO), and E_2 (low) modes adjacent to the source-connected field plate (SCFP) in the gate-drain access region. Measurements of the pinched OFF state were taken at a gate bias of V_{gs} = −5 V, while the drain bias was increased from V_{ds} = 0 V to 40 V. In the next experiment in the ON state, the gate bias was set to V_{gs} = −2.85 V (required to keep the current below the SMU current compliance of 100 mA), while the drain bias was increased from V_{ds} = 0 V to 40 V. In the pinched OFF state, the drain and gate leakage currents were both less than 6 μA/mm so that the temperature rise due to self-heating was negligible. The changes in the Raman peak positions of the E_2 (high), A_1 (LO), and E_2 (low) modes for the DUT biased in the pinched OFF state and ON state are shown in Fig. 4. Typical uncertainties (95% confidence intervals) for the change in Raman peak positions $\Delta\omega = \omega(V_{ds} \geq 0) - \omega(V_{ds} = 0)$ were ±0.01 cm^{-1} for the E_2 (high) and E_2 (low) modes and ±0.05 cm^{-1} or lower for the A_1 (LO) mode. For the measurements shown in Fig. 4, we treated $\omega(V_{ds} \geq 0)$ and $\omega(V_{ds} = 0)$ as independent measurands to calculate the 95% confidence intervals from the standard deviation of ten spectra collected at each drain bias point.

In the pinched OFF state measurements shown in Fig. 4(a), the frequencies of E_2 (high) and E_2 (low) peaks increased while the frequency of the A_1 (LO) peak decreased, similar to our previous work.[17] This is because a positive drain bias $V_{ds} \geq 0$ V induces a negative electric field component E_z along the c-axis in the gate-drain access region, which shortens and stiffens the Ga–N bond along the c-axis

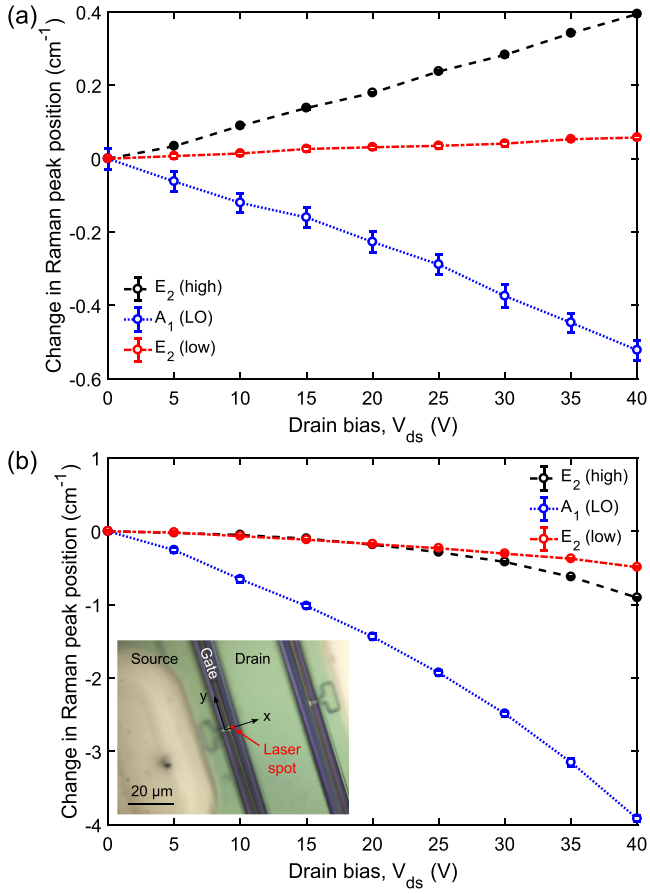

FIG. 4. Change in the Raman peak positions with drain bias for (a) the pinched OFF state at V_{gs} = −5 V and (b) the ON state at V_{gs} = −2.85 V. The error bars represent 95% confidence intervals on the change in peak position $\Delta\omega = \omega(V_{ds} \geq 0) - \omega(V_{ds} = 0)$ with $\omega(V_{ds} \geq 0)$ and $\omega(V_{ds} = 0)$ treated as independent measurands. The inset of (b) shows an optical microscope image of the DUT with the measurement spot in the gate-drain access region.

(resulting in $\Delta\omega_{A_1(LO)} < 0$) and lengthens and relaxes the Ga–N bonds in the c-plane (resulting in $\Delta\omega_{E_2(h)}, \Delta\omega_{E_2(\ell)} > 0$). The magnitudes of the frequency shifts differ owing primarily to the difference in electric field coefficients B for each mode listed in Table I with $|B_{E_2(\ell)}| < |B_{E_2(h)}| < |B_{A_1(LO)}|$. For the ON state measurements shown in Fig. 4(b), the frequencies of all three peaks decrease, primarily because of the negative values of the temperature coefficient A for all three modes listed in Table I. The A_1 (LO) mode shows the sharpest decrease in frequency with drain bias because of the combined effects of larger temperature and electric field coefficients and a smaller biaxial stress coefficient than the E_2 (high) mode. The E_2 (high) mode and E_2 (low) mode show a coincidentally similar frequency shift from V_{ds} = 0 V to 20 V due to the complex contributions of temperature rise, in-plane stress, and vertical electric field with different coefficients for each mode. Beyond V_{ds} = 20 V, however, the frequency of the E_2 (high) mode decreases more rapidly due to the stronger influence of the temperature rise on the phonon frequency.

Although it is often not explicitly discussed in the micro-Raman thermometry literature, most reports of micro-Raman thermometry in GaN HEMTs have assumed that the

temperature, stress, and/or electric field measured by the Raman peak shifts represent the averages of these quantities through the thickness of the GaN buffer across an ≈1 μm diameter spot. Beechem[36] validated and Bagnall *et al.*[16] examined this assumption for the temperature and IPE strain, respectively, and found it to be correct for typical temperature and strain gradients in the GaN buffer. In this work, we note that this assumption of depth averaging through the GaN buffer is particularly important as it relates to the vertical electric field $E_z = E_z(x,z)$, which is known to vary significantly along the channel and through the thickness of the GaN buffer. At a particular point x along the channel, the depth-averaged vertical electric field by definition is given by the potential difference across the buffer divided by the thickness of the buffer L_b,

$$\bar{E}_z(x) = \frac{1}{L_b}\int_{-L_b}^{0} E_z(x,z)\,dz = \frac{1}{L_b}\int_{-L_b}^{0} -\frac{\partial\varphi(x,z)}{\partial z}dz$$

$$= -\frac{\varphi(x,0) - \varphi(x,-L_b)}{L_b}, \tag{7}$$

regardless of the spatial variation of $E_z(x,z)$ with z. This is a crucial statement as it suggests that measurement of the average vertical electric field can experimentally assess the potential difference across the GaN buffer and probe its electrostatic behavior, which we discuss further in Sec. IV A and the Appendix.

IV. MODELING

To support our experimental measurements of the temperature, stress, and electric field described in Sec. III, we developed an uncoupled electro-thermo-mechanical model of the GaN HEMT using the Silvaco ATLAS/BLAZE[37] and COMSOL Multiphysics[38] finite element analysis (FEA) software packages. First, we computed the 2D electric potential $\varphi(x,z)$ and power dissipation $\dot{Q}_v(x,z)$ distributions with a self-consistent electro-thermal model in Silvaco ATLAS/BLAZE. Then, we imported φ and $\dot{Q}_v$ into a 3D electro-thermo-mechanical model in COMSOL Multiphysics including the thermoelastic and piezoelectric effects to compute the temperature, stress, and electric field. We chose this uncoupled, two-step modeling approach because of the prohibitive computational cost of modeling a multifinger GaN HEMT with full coupling of the stress tensor with semiconductor device electrostatics[4] and because of our focus on validating micro-Raman measurements of the GaN buffer rather than the dependence of the HEMT operation on the electro-mechanical state of the AlGaN barrier. The accuracy of our uncoupled model is supported by the principle that the relatively small mechanical stresses ($\lesssim$200 MPa) induced by the thermoelastic and IPE effects will not significantly change the electric field distribution since the peak electric field magnitudes are already very large in GaN HEMTs (~2 MV/cm). These two steps and their results are described in more detail in Secs. IV A and IV B.

A. 2D semiconductor device model

Semiconductor device modeling of GaN HEMTs is often challenging because of an incomplete knowledge of the device structure and material properties, the strong sensitivity of the results on the material properties and constitutive relations (many of which differ among experimental reports or are only available by modeling), non-ideal effects introduced during device fabrication, and variability among a population of devices.[39,40] In practice, one frequently adjusts the values of certain parameters in order to match the current-voltage characteristics of the model to those measured on one or more devices. While this "calibration" of the semiconductor device model limits the predictive capability of the model, it is a practical necessity due to the complex physics of semiconductor devices, especially for a less mature technology like GaN HEMTs. In our 2D electro-thermal model implemented in Silvaco ATLAS/BLAZE, we have limited the number of adjustable parameters to two (AlGaN barrier thickness and ohmic contact resistance) in order to match the measured transfer ($I_d - V_{gs}$) and output characteristics of the DUT, which we describe in more detail in the following paragraphs. The key results of this model are the electric potential, vertical electric field $E_z = -\partial\varphi/\partial z$, and power dissipation distributions as inputs to the 3D electro-thermo-mechanical model that are more accurate than if we assumed their spatial distribution *a priori*.

The semiconductor device model was implemented in Silvaco ATLAS/BLAZE with the drift-diffusion model and both electron and hole current continuity equations. Self-heating of the HEMT was self-consistently accounted for in the model through the GIGA module with the power dissipation due to Joule heating $\dot{Q}_v = \vec{J}\cdot\vec{E}$ and temperature-dependent material properties. We believe the drift-diffusion transport model to be sufficiently accurate for the purposes of this work because we observed the heat generation region to extend ≈0.2 μm–1 μm along the channel (depending on the drain bias), whereas velocity overshoot in wurtzite GaN occurs over distances of ≈0.1 μm.[41] The HEMT geometry and epitaxy dimensions were taken from the values published by the manufacturer[35] or cross-sectional SEM images. The energy band parameters,[42] temperature- and electric field-dependent electron mobility relations,[43] and dielectric constants[30,45] for AlN, AlGaN, GaN, and 4H–SiC were taken from various references in the literature. The properties of the $Al_{0.22}Ga_{0.78}N$ barrier were interpolated between the properties of AlN and GaN using Vegard's rule (linear average) except for the bandgap, for which the recommended bowing parameter of $C = 0.7$ was used.[42] The electron mobility of the two-dimensional electron gas (2DEG) was assigned a value of 2000 cm^2/V s at room temperature[35] with an electric field-dependence from Monte Carlo simulations[46] and a temperature dependence of $\sim T^{-2.5}$ from measurements in the literature,[47] where T is the absolute temperature in kelvin.

The thermal conductivity values of GaN ($k_{300} = 170$ W/m K[48]) and 4H–SiC ($k_{xy,300}$ = 490 W/m K and $k_{zz,300}$ = 390 W/m K[49]) with their temperature dependencies of $\sim T^{-n}$ ($n = 1.44$ for GaN[48] and $n = 1.49$ for 4H–SiC[50]) were also taken from the literature. The thermal conductivity of the ≈50 nm thick AlN nucleation layer was set to 10 W/m K to provide a GaN–SiC thermal boundary resistance (TBR) of 5×10^{-9} m^2 K/W[51] that is temperature-independent.[48] The thermal conductivity of the AlGaN barrier was assigned an approximate

value of 10 W/m K to account for the significant reduction in thermal conductivity compared to AlN and GaN due to alloying[52] and mean free path suppression effects owing to its ≈20 nm thickness.[53] Finally, the thermal conductivity of the Ag-filled epoxy was set to a constant value of 7 W/m K as reported by the manufacturer.[54]

Our methodology for reproducing the measured current-voltage characteristics of the DUT with the ATLAS/BLAZE model was to match the measured and modeled transfer characteristics shown in Fig. 5 at V_{ds} = 0.1 V by adjusting the gate threshold voltage (V_{th}) and drain current (I_d) through the AlGaN barrier thickness and ohmic contact resistance. The gate threshold voltage is strongly affected by both the polarization sheet charge at the AlN/GaN interface and the AlGaN barrier thickness; thus, one could modify either or both of these quantities to obtain the experimentally measured V_{th} = −3.3 for the DUT. We chose to fix the polarization sheet charge at the AlN/GaN interface to the value of $+1.17 \times 10^{13}$ cm^{-2} predicted by the difference in polarization between $Al_{0.22}Ga_{0.78}N$ and GaN[55] and the measured residual stress of the GaN buffer of our DUT, resulting in a 2DEG concentration of $n_s = 9.5 \times 10^{12}$ cm^{-2} within the expected range.[35] The Schottky barrier height of the gate contact was set to ϕ_B = 1.1 eV, which is typical for the Ni/Pt/Au gate metallization at Al mole fractions of ≈0.22.[55,56] Although the manufacturer of the DUT we tested reported an AlGaN barrier thickness of 25 nm as typical in their device structures,[35] its exact thickness in our sample is unknown. We know that other AlGaN/GaN-on-SiC epitaxial structures from the same manufacturer have AlGaN thicknesses as small as 16 nm and found that setting the AlGaN barrier thickness to 19 nm for our DUT correctly reproduced the measured threshold voltage of ≈−3.3 V. Then, we added an ohmic contact resistance to the source and drain contacts to reduce the drain current to its experimentally measured value of 35 mA at V_{ds} = 0.1 V and V_{gs} = 0 V. Unfortunately, we were not able to experimentally validate the ohmic contact resistance value for this DUT because this device did not include transmission line method (TLM) structures needed to independently measure the contact resistance. We found the output characteristics measured at V_{gs} = −2.85 V from

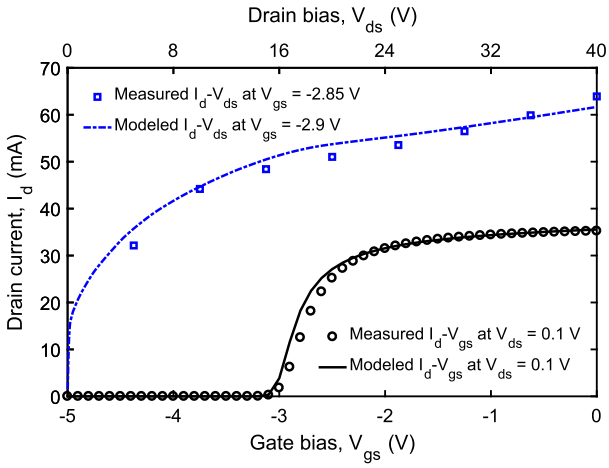

FIG. 5. Measured and modeled transfer characteristics ($I_d - V_{gs}$) at V_{ds} = 0.1 V and output characteristics ($I_d - V_{ds}$) at V_{gs} = −2.85 V.

V_{ds} = 0 to 40 V (the ON state condition of our micro-Raman measurements) agreed well with the ATLAS/BLAZE model at V_{gs} = −2.9 V as shown in Fig. 5 (the slight adjustment of the gate bias in the model improved the agreement with the measurements).

One critical issue in the ATLAS/BLAZE model as it relates to the vertical electric field E_z across the GaN buffer is the influence of traps, impurities, or deep levels (intentional dopants or unintentional contaminants) on the electrostatic behavior of the buffer. As we discuss in greater detail in the Appendix, the presence of intentional iron (Fe) doping and unintentional carbon (C), oxygen (O), and Si incorporation results in either a highly resistive n-type or a highly resistive p-type GaN buffer, depending on the relative concentrations of Fe and C as deep acceptors and Si and O as shallow donors. When the concentration of substitutional carbon at the nitrogen site [C_N] is greater than the total shallow donor concentration N_D, the Fermi level in the bulk of the GaN buffer is pinned near the C_N trap energy level (0.9 eV above the valence band[57]), resulting in a highly resistive p-type GaN buffer and the buffer-drain acting as a reverse biased p-n junction.[58] When N_D is greater than [C_N] but less than [C_N] + [Fe], where [Fe] is the Fe doping concentration, the Fermi level in the bulk of the GaN buffer is pinned just below the Fe deep acceptor energy level (0.7 eV below the conduction band[58,59]), resulting in a highly resistive n-type GaN buffer. In the case of a p-type GaN buffer, essentially all of the increase in electric potential φ due to increasing the drain bias V_{ds} occur across the GaN buffer until the buffer is depleted as predicted by standard p-n junction theory.[60] Therefore, the depth-averaged vertical electric field across the GaN buffer between V_{ds} = 0 and $V_{ds} \geq 0$ at the same gate bias is approximately $\bar{E}_z = -V_{ds}/L_b$ according to Eq. (7). However, when the GaN buffer is a semi-insulating n-type material, the drain and source can communicate electrostatically by freely changing the electron quasi-Fermi level of the buffer, resulting in a lateral potential drop from drain to source and average vertical electric field $|\bar{E}_z| < V_{ds}/L_b$. Both cases are depicted by Figs. 6(a) and 6(b) calculated with the ATLAS/BLAZE model for [C_N] = 10^{17} cm^{-3}, $N_D = 7 \times 10^{16}$ cm^{-3} or $N_D = 1.1 \times 10^{17}$ cm^{-3}, and a typical graded Fe doping profile varying from [Fe] = 3.6×10^{16} cm^{-3} at the channel to 3×10^{18} cm^{-3} at 0.8 μm depth into the buffer.[61]

As shown by the potential distributions $\varphi(x,z)$ in Figs. 6(a) and 6(b), the electrostatic behavior of the buffer is strongly affected by its p-type or n-type character, even if it is semi-insulating in both cases. Because the average vertical electric field in the pinched OFF state derived from the micro-Raman measurements shown in Fig. 4 and analyzed in Sec. V A closely follows the p-type buffer case when [C_N] > N_D, we proceeded to use the ATLAS/BLAZE model with the p-type buffer for the remainder of the modeling in Sec. IV B and comparison to the experimental data in Sec. V. We also plotted the difference in electric potential between V_{ds} = 0 V and V_{ds} = 40 in the ON state at V_{gs} = −2.9 in Fig. 6(c), which is very similar to the electric potential difference in the pinched OFF state shown in Fig. 6(a) except very near the edge of the gate-connected field plate. Hence, our ATLAS/BLAZE model

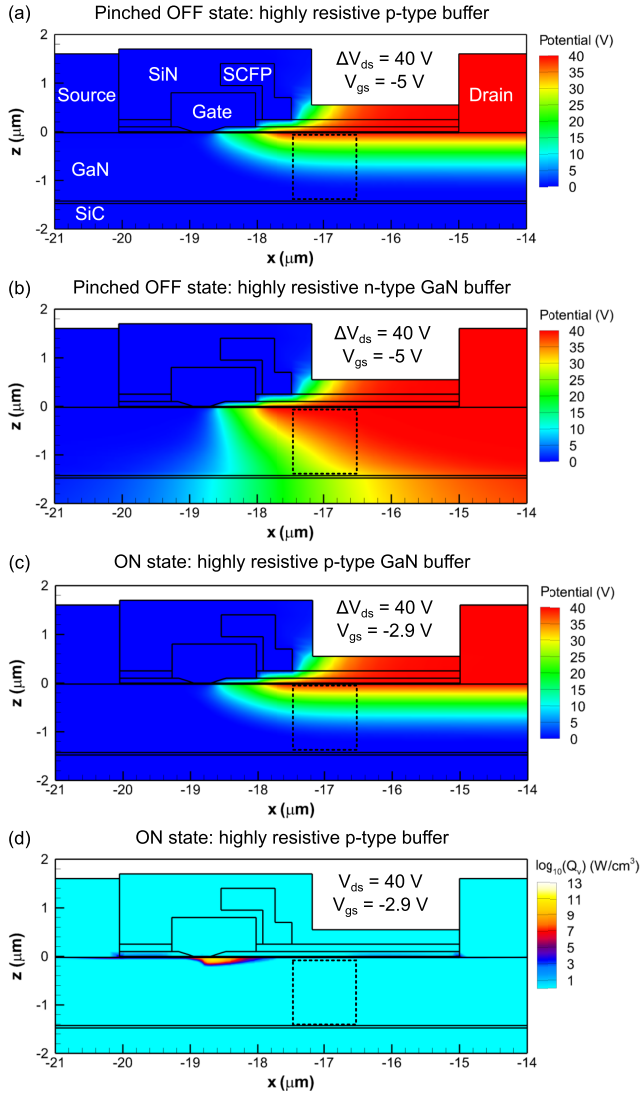

FIG. 6. ATLAS/BLAZE modeling results for the difference in electric potential φ between V_{ds} = 40 V and V_{ds} = 0 V in the (a) pinched OFF state (V_{gs} = −5 V) for the highly resistive p-type buffer when $[C_N] > N_D$, (b) pinched OFF state (V_{gs} = −5 V) for the highly resistive n-type buffer when $[C_N] < N_D$, (c) ON state (V_{gs} = −2.9 V) for the highly resistive p-type buffer, and (d) the ON state dissipated power density at V_{ds} = 40 V and V_{gs} = −2.9 V. The dotted rectangle indicates the micro-Raman collection volume in the experiment.

supports the prior hypothesis[11] and our experimental finding in Sec. V B that the average vertical electric field in the gate-drain access region is approximately the same whether the channel is open or closed. Finally, the dissipated power density $\dot{Q}_v$ in the ON state at V_{ds} = 40 V and V_{gs} = −2.9 V used as the input for determining the temperature rise in the COMSOL Multiphysics model in Sec. IV B is shown in Fig. 6(d). The majority of the total dissipated power occurs in an ≈1 μm region adjacent to the intrinsic gate in the gate-drain access region due to depletion of the 2DEG in this region.

B. 3D electro-thermo-mechanical device model

With the electric potential and dissipated power density distributions calculated by the 2D ATLAS/BLAZE as the inputs, we developed a 3D electro-thermo-mechanical model of the DUT in COMSOL Multiphysics to compute the temperature rise and mechanical stress induced by self-heating and the thermoelastic and inverse piezoelectric effects. These 2D distributions in the (x,z) plane were set to constant values over the gate width direction (y) and zero in the inactive region beyond the extent of the gate. This COMSOL model first solved the steady-state heat conduction equation

$$\nabla \cdot (k\nabla T) + \dot{Q}_v = 0, \tag{8}$$

to find the temperature distribution $T(x,y,z)$ from the dissipated power density and then solved the static equilibrium equation

$$\nabla \cdot \sigma_{ij} = 0 \tag{9}$$

subject to the constitutive relation for piezoelectric and thermoelastic solids,

$$\epsilon_{ij} = S_{ijkl}\sigma_{kl} + d_{kij}E_k + \alpha_{ij}\Delta T, \tag{10}$$

where ϵ_{ij} and σ_{ij} are the strain and stress tensors, E_k is the electric field vector, S_{ijkl} is the elastic susceptibility tensor, d_{kij} is the piezoelectric modulus tensor, and α_{ij} is the coefficient of thermal expansion tensor.[62]

The elastic and piezoelectric properties of GaN,[30] AlN,[44] and 4H–SiC[63,64] were taken from the literature, and the elastic modulus and Poisson ratio of the Ag-filled epoxy were estimated to be E = 1 GPa[65] and ν = 0.3. To limit the complexity of this large-scale 3D model, the AlGaN barrier, the AlN interlayer, gate metallization, and field plates were not included in the COMSOL model. We did include the SiN passivation and gold (Au) source and drain metallization for which we used the default properties in COMSOL Multiphysics. Although the thermal and mechanical properties of SiN passivating layers may vary depending upon the deposition method, they do not strongly affect the temperature and stress in the GaN buffer because the primary heatsinking and mechanical clamping of the buffer is provided by the SiC substrate.

For the mechanical boundary conditions, the bottom of the Ag-filled epoxy die-attach was set to zero displacement and the sides and top of the HEMT die set to free boundaries (zero stress). For the thermal boundary conditions, the sides and top of the HEMT die were also set to adiabatic (thermally insulated) boundaries to model the negligible heat transfer by natural air convection. Initially, we set the thermal boundary condition at the bottom of the epoxy die-attach to a finite conductance equivalent to a thermal resistance of 5.7 °C/W to account for the conduction resistance of the QFN package paddle, the lead tin (Sn63/Pb37) solder via under the DUT, and the copper block. However, we found that the modeled temperature rise was lower than the measured temperature rise using the E_2 (high) and A_1 (LO) modes with the pinched OFF state taken as the unpowered reference according to Eq. (2), which suggests that there is an additional thermal resistance between the die-attach and the TEC maintained at 20 ± 0.1 °C. Therefore, we increased the thermal resistance between the bottom of the epoxy die-attach and the ambient in the model to 41.9 °C/W to match the experimental temperature rise at one data point (V_{ds} = 20 V, V_{gs} = −2.85 V, and P_{diss} = 1.02 W) and kept this value fixed for all of the remaining simulations, similar to Ref. 66. The source of this additional thermal resistance may

be incomplete filling of the solder via and thermal contact resistances between the QFN paddle, solder via, and copper block due to the limited packaging capabilities in our laboratory. However, as the E_2 (high)/A_1 (LO) two-peak fit method has already been validated quantitatively by Choi *et al.*[14] for a GaN HEMT with a more well-controlled package structure, we believe that this approach is appropriate. Contour plots of the vertical electric field, IPE stress, temperature rise, and total stress are shown in Fig. 7 at V_{ds} = 40 V in the pinched OFF state at V_{gs} = −5 V and in the ON state at V_{gs} = −2.9 V.

As discussed in our previous work concerning the vertical electric field in GaN HEMTs measured by micro-Raman,[17] the vertical electric field in the gate-drain access region and under the drain contact plotted in Fig. 7(a) for the pinched OFF state is negative (pointing from the top to the bottom of the GaN buffer) owing to the decreasing electric potential from the top to the bottom of the buffer. The $E_z(x,z)$ profile is piecewise linear with depth z (not exponential as discussed in Ref. 67) since the buffer-drain acts as a reverse-biased p-n junction when

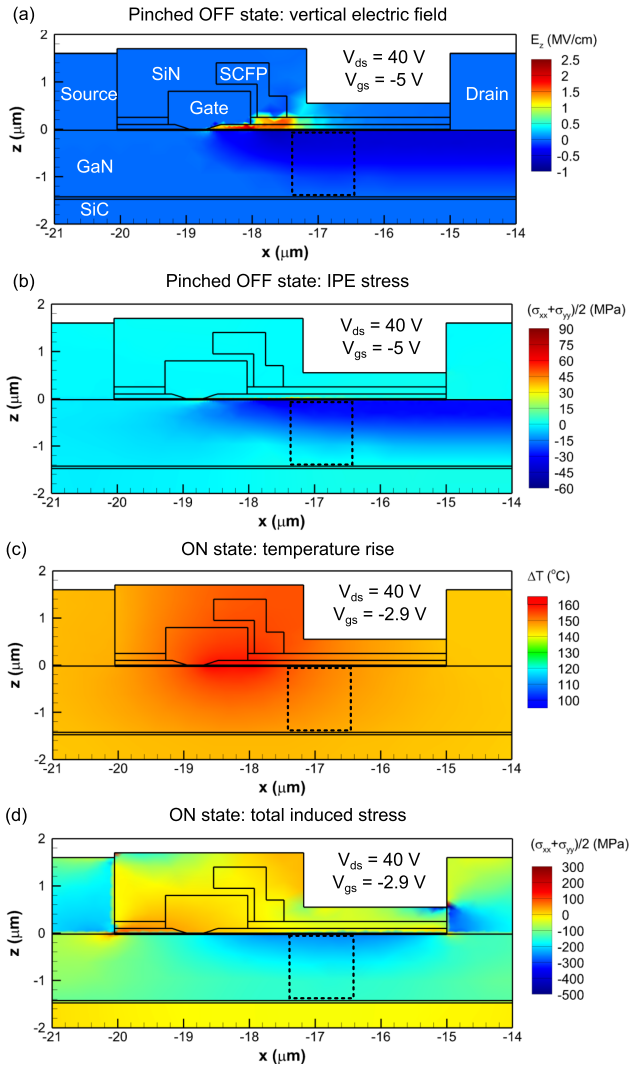

FIG. 7. (a) Vertical electric field and (b) IPE stress in the pinched OFF state at V_{ds} = 40 V and V_{gs} = −5 V. (c) Temperature rise and (d) total induced stress in the ON state at V_{ds} = 40 V and V_{gs} = −2.9 V for the highly resistive p-type buffer or $[C_N] > N_D$. The dotted rectangle indicates the micro-Raman collection volume in the experiment as in Fig. 6.

$[C_N] > N_D$ and is only weakly dependent on distance along the channel x beyond the edge of the source-connected field plate (SCFP). Because the vertical electric field is confined to the SiN passivation, AlGaN barrier, and GaN buffer and because the GaN buffer is piezoelectric and substantially thicker than the passivation and barrier, the induced IPE stress shown in Fig. 7(b) is primarily confined to the GaN buffer. The IPE stress in the buffer is compressive (σ_{xx},σ_{yy} < 0), piecewise linear with depth, and weakly dependent on distance along the channel in the gate-drain access region as it is approximately proportional to the local vertical electric field.[16]

The temperature rise in the ON state plotted in Fig. 7(c) is highest at the edge of the gate on the same side as the drain due to the concentration of dissipated power in that area [see Fig. 6(d)] and decreases with distance away from the HEMT channel. In this DUT, the temperature rise is fairly uniform in the GaN buffer because of the relatively high thermal resistance of the die-attach and package. The total stress shown in Fig. 7(d) is compressive due to the compressive contributions of the IPE and thermoelastic stresses in the ON state. The larger coefficient of thermal expansion of GaN compared to 4H–SiC and SiN and the higher temperature of the GaN buffer are responsible for the compressive thermoelastic stress, which reaches its maximum value at the top of the buffer and varies slightly with depth in the buffer.

V. RESULTS AND ANALYSIS

A. Pinched OFF state

The theory developed in our previous work[17] and in Sec. II of this work leading to Eq. (6) proposes that the vertical electric field and in-plane IPE stress can be self-consistently measured in the pinched OFF state from the changes in peak positions of the E_2 (high) and A_1 (LO) modes according to

$$\begin{bmatrix} (\sigma_{xx}+\sigma_{yy})/2 \\ E_z \end{bmatrix}_{\Delta T=0} = \begin{bmatrix} K_{E_2(h)} & B_{E_2(h)} \\ K_{A_1(LO)} & B_{A_1(LO)} \end{bmatrix}^{-1} \begin{bmatrix} \Delta\omega_{E_2(h)} \\ \Delta\omega_{A_1(LO)} \end{bmatrix}, \tag{11}$$

under the assumption of zero temperature rise. However, we have uniquely proposed in this work that the temperature rise, the in-plane stress, and the vertical electric field can be measured simultaneously with a similar system of equations derived from Eq. (5),

$$\begin{bmatrix} \Delta T \\ (\sigma_{xx}+\sigma_{yy})/2 \\ E_z \end{bmatrix} = \begin{bmatrix} A_{E_2(h)} & K_{E_2(h)} & B_{E_2(h)} \\ A_{A_1(LO)} & K_{A_1(LO)} & B_{A_1(LO)} \\ A_{E_2(\ell)} & K_{E_2(\ell)} & B_{E_2(\ell)} \end{bmatrix}^{-1} \begin{bmatrix} \Delta\omega_{E_2(h)} \\ \Delta\omega_{A_1(LO)} \\ \Delta\omega_{E_2(\ell)} \end{bmatrix}, \tag{12}$$

from the changes in peak positions of the E_2 (high), A_1 (LO), and E_2 (low) modes. Although Eq. (5) is written for the ON state ($V_{gs} > V_{th}$), it is equally valid to apply it to the pinched OFF state ($V_{gs} < V_{th}$) because it is derived directly from Eqs. (3) and (4). If Eqs. (11) and (12) are correct, the in-plane stress and vertical electric field values obtained from the two-peak fit and three-peak fit should be the same with the three-peak fit yielding $\Delta T \approx 0$. We have analyzed the measured

changes in Raman peak positions shown in Fig. 4(a) and plotted the vertical electric field, the average in-plane IPE stress, and the temperature rise using these two experimental methods in Fig. 8 along with the 3D electro-thermo-mechanical modeling results. For the modeled values of these quantities, we averaged the values over the 1 μm region adjacent to the source-connected field plate in the gate-drain access region through the thickness of the GaN buffer that corresponds to the micro-Raman measurement location in the experiment. For the values of the temperature coefficients, we have used the experimental values measured in this work listed in Table I. For the stress and electric field coefficients, we have used the values calculated by DFT in this work, which are also listed in Table I. The error bars on the experimental values represent 95% confidence intervals calculated from the random errors associated with multiple measurements of the Raman peak positions and the uncertainty in the temperature shift coefficients A_n stated in Table I.

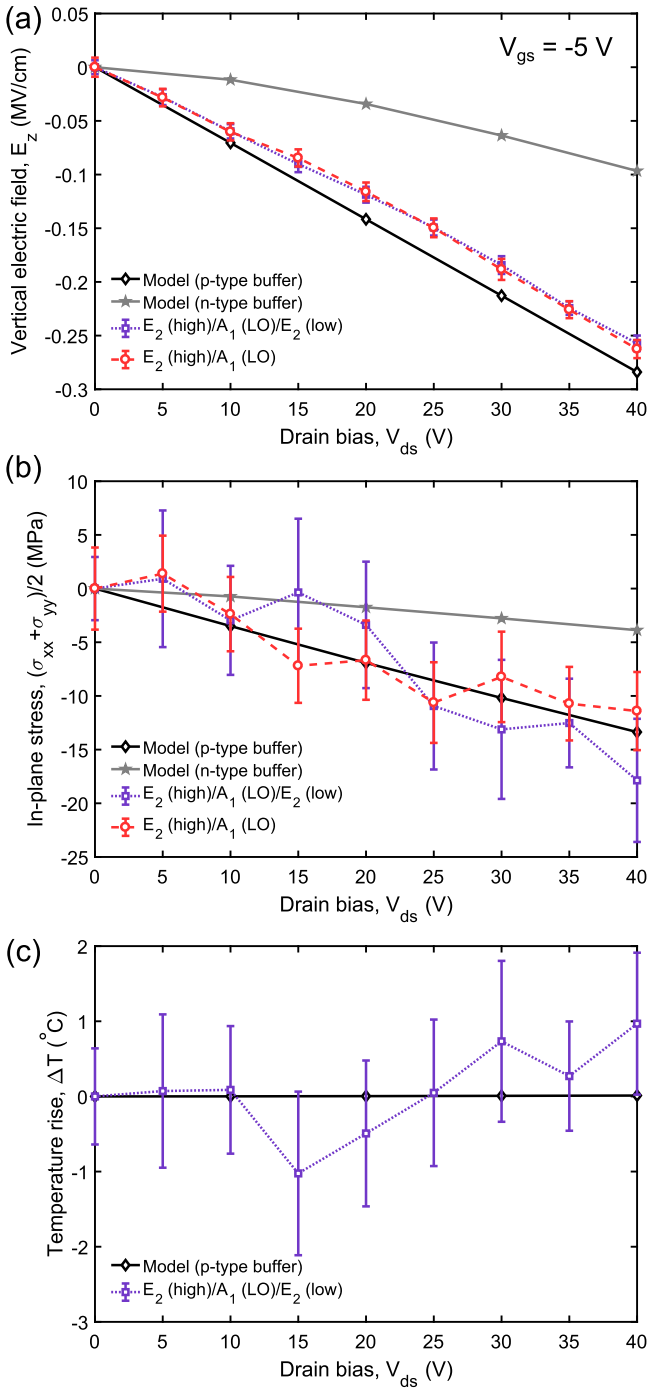

FIG. 8. (a) Vertical electric field, (b) in-plane IPE stress, and (c) temperature rise in the pinched OFF state (V_{gs} = −5 V) as a function of drain bias from the electro-thermo-mechanical model and micro-Raman measurements. The error bars on the experimental values represent 95% confidence intervals calculated from the random errors associated with multiple measurements of the Raman peak positions and the uncertainty in the temperature shift coefficients A_n stated in Table I.

Both the experimental and modeling results for the vertical electric field in Fig. 8(a) show that E_z is negative and increases in magnitude with increasing drain bias, similar to our previous work introducing the two-peak fit method in the pinched OFF state.[17] The E_z values extracted from the two experimental methods (two-peak and three-peak) agree within 5% of each other and lie between the two bounds of the electro-thermo-mechanical model for $[C_N] > N_D$ (p-type buffer) and $[C_N] < N_D$ (n-type buffer) as expected. The experimental E_z values are closer to the p-type buffer case (≈15% lower than the modeled values), which suggests that the GaN buffer in our DUT is a highly resistive p-type material. The average in-plane stress shown in Fig. 8(b) is compressive with values in the range of −10 MPa to −20 MPa at V_{ds} = 40 V and slightly better agreement for the two-peak fit method given by Eq. (11). The measured stress values show more deviation from a linear trend and have higher relative uncertainties than the measured vertical electric field because less than 20% of the change in Raman peak positions is due to the in-plane stress (>80% is due to E_z). We also find that the temperature rise derived from the three-peak fit method given by Eq. (12) and shown in Fig. 8(c) is ±1 °C with most of the error bars crossing the line $\Delta T = 0$. Thus, the three-peak method to simultaneously measure the vertical electric field, in-plane stress, and temperature rise yields the same vertical electric field and in-plane stress as the two-peak method and negligible temperature rise, even in the presence of significant Raman peak shifts ($|\Delta\omega| \geq 0.5$ cm^{-1}).

B. ON state

The success of the three-peak fit method given by Eq. (12) in properly decoupling the vertical electric field, in-plane stress, and temperature rise in the pinched OFF state in Sec. V A suggests that the same methodology can properly measure these quantities in the ON state at any gate and drain bias. Therefore, we have extracted the temperature rise, in-plane stress, and vertical electric field from the changes in peak positions of the three peaks for the ON state measurements in Fig. 4(b) based on Eqs. (5) and (12) and compared the results to our 3D electro-thermo-mechanical model in Fig. 9. To further validate the three-peak fit method in the ON state, we have also plotted the temperature rise and in-plane thermoelastic stress derived by the two-peak fit method introduced by Choi *et al.*[14] using the pinched OFF measurements as the reference according to Eq. (2). As in Fig. 8, the error bars on the experimental values in Fig. 9 represent 95% confidence intervals calculated from the random errors

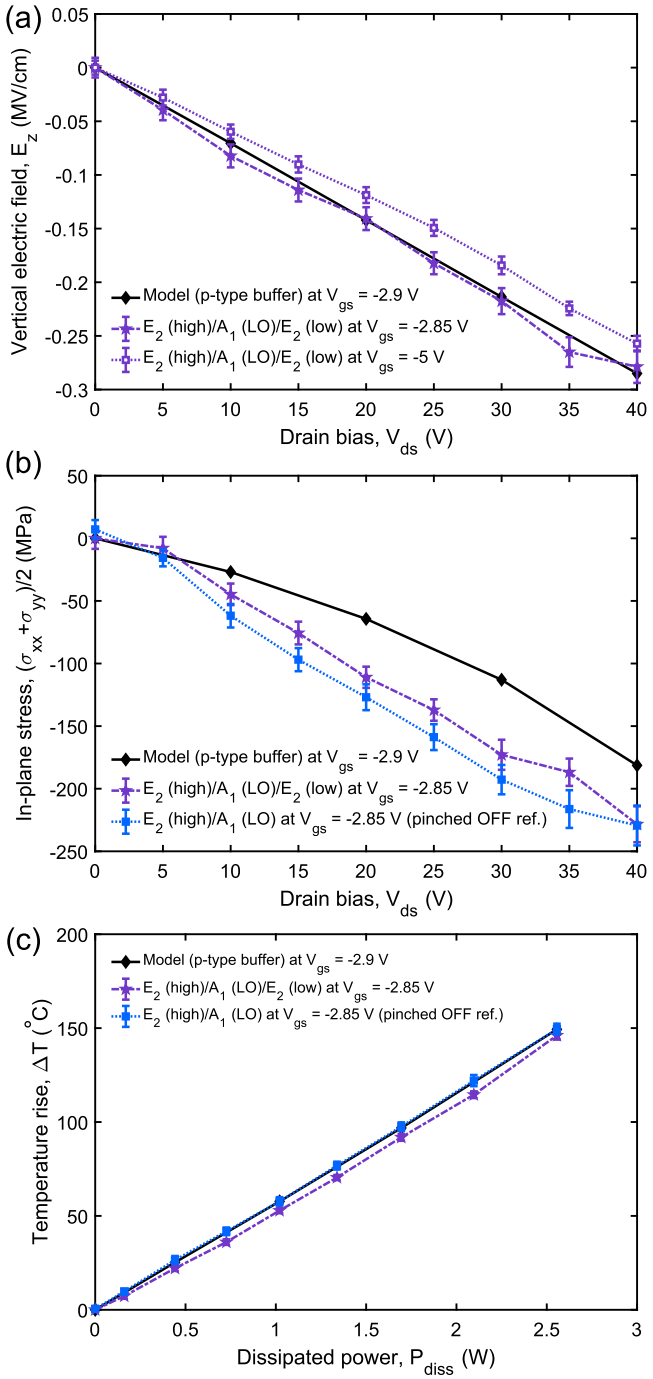

FIG. 9. (a) Vertical electric field, (b) in-plane stress, and (c) temperature rise in the ON state as a function of the drain bias measured at V_{gs} = −2.85 V. The measured results obtained by the three-peak fit method are compared to the electro-thermo-mechanical model and the two-peak fit method using the pinched OFF measurements as the reference. The error bars on the experimental values represent 95% confidence intervals calculated from the random errors associated with multiple measurements of the Raman peak positions and the uncertainty in the temperature shift coefficients A_n stated in Table I.

of multiple measurements of the Raman peak positions and the uncertainty in the temperature coefficients A_n stated in Table I.

The vertical electric field extracted from the ON state measurements plotted in Fig. 9(a) shows the same behavior as in the pinched OFF state (negative values and increasing magnitude with drain bias) but even better agreement with the modeled values for a p-type buffer. The ATLAS/BLAZE model suggests that the potential difference across the GaN buffer at the micro-Raman measurement location should be approximately the same regardless of whether the channel is open (ON state) or closed (pinched OFF state). Supporting this idea, we do find good agreement (within ≈15%) between the measured E_z values in the ON state and pinched OFF state despite the significant temperature rise and in-plane stress in the ON state induced by self-heating. The measured in-plane stress, which is the total stress or sum of the IPE and thermoelastic stress in the ON state, follows the expected trend of increasingly compressive values with increasing drain bias. The measured total in-plane stress values in the ON state shown in Fig. 9(b) are ≈25% higher than the modeled values. The measured in-plane stress values obtained using the two-peak fit method with the pinched OFF state as the unpowered reference, which should only be the thermoelastic stress, also plotted in Fig. 9(b), are ≈20 MPa larger in magnitude than the total stress from the three-peak method. This is not expected because the total stress should be more compressive (higher magnitude) than the thermoelastic stress due to the fact that the IPE and thermoelastic stresses are both compressive. The temperature rise extracted from the three-peak fit method in Fig. 9(c) increases with increasing drain bias and dissipated power as expected with values 5 °C–10 °C lower than the two-peak fit method. The two-peak fit method shows very good agreement with the 3D electro-thermo-mechanical model, in part because the unknown thermal resistance between the bottom of the epoxy die-attach was fitted to the measured temperature rise at V_{ds} = 20 V and kept constant for all of the remaining simulations.

Despite the minor disagreements between the three-peak fit method introduced in this work and the two-peak fit method previously introduced in the pinched OFF state[17] and the ON state,[14] the simultaneous measurement of the vertical electric field, in-plane stress, and temperature rise via the three-peak fit method yields good quantitative results and a number of physical insights into GaN HEMTs and their characterization by micro-Raman spectroscopy. First, we believe that the measurement of the average vertical electric field across the buffer, which is proportional to the electric potential difference, can identify whether the buffer is highly resistive p-type or n-type material when compared to a semiconductor device model. Together with DC and RF measurements of the transistor and elemental analysis via secondary ion mass spectroscopy (SIMS), our Raman-based electric field measurement helps us to identify how the electrostatics of the buffer influenced by the presence of impurities (C, Fe, O, Si, etc.) affect charge trapping and RF performance in GaN HEMTs. Second, we have provided a systematic explanation supported by experiment that describes which quantities are measured by micro-Raman spectroscopy of GaN HEMTs under bias. We have confirmed that the vertical electric field is the same in the pinched OFF state and the ON state, which supports the hypothesis that the effect of the vertical electric field and IPE stress on the Raman spectrum in the ON state is removed by using the pinched OFF state as the unpowered reference. This is further supported by similar temperature and in-plane stress values obtained in the ON state using the two-peak and three-peak fit methods.

C. Additional Considerations

In our analysis of the experimental data and comparison to the electro-thermo-mechanical model, we have assumed that the measured temperature, stress, and electric field values represent the volumetric average of these quantities over the micro-Raman collection volume ($\approx 1 \times 1\ \mu m^2$ through the thickness of the GaN buffer) as is common in the micro-Raman thermometry literature.[8–14] Due to the significant spatial variation of primarily the vertical electric field and in-plane stress distributions seen in Fig. 7 from our model, we sought to validate this assumption. One approach to validating the volumetric average assumption is to model the aggregate Raman spectrum $I(\omega)$ from which the Raman peak position ω is determined as the sum of Raman spectra from each differential volume $d^3\vec{r}$,

$$I(\omega) = \int L(\omega; \mu(\vec{r}), \Gamma(\vec{r}))d^3\vec{r}, \tag{13}$$

where $L(\omega; \mu(\vec{r}), \Gamma(\vec{r}))$ represents the Lorentzian lineshape of the intrinsic Raman spectrum from an elemental volume at location $\vec{r} = x\hat{i} + y\hat{j} + z\hat{k}$ with centroid μ and linewidth Γ.[16] We extracted the vertical electric field $E_z(\vec{r})$, stress $\sigma_{ij}(\vec{r})$, and temperature rise $\Delta T(\vec{r})$ distributions from the 3D electro-thermo-mechanical model in COMSOL Multiphysics and simulated the aggregate Raman spectrum using Eq. (13) for the E_2 (high) mode by calculating $\mu(\vec{r}) - \mu_0$ with Eq. (3) and a nominal value of $\Gamma = 2\ cm^{-1}$ at $V_{ds} = 40$ V. From this calculation, we obtained a simulated Raman peak position shift of $\Delta\omega_{E_2(h)}$ that differed by less than 1% from the volumetric averaging assumption $\Delta\omega_{E_2(h)} = K_{E_2(h)}\left(\bar{\sigma}_{xx} + \bar{\sigma}_{yy}\right)/2 + B_{E_2(h)}\bar{E}_z + A_{E_2(h)}\Delta\bar{T}$ in both the pinched OFF state and the ON state. The peak position shifts $\Delta\omega_n$ for the A_1 (LO) and E_2 (low) modes also show errors of less than 1% with the volumetric averaging assumption. Thus, we also believe that the quantities measured in the GaN buffer from the changes in the Raman peak positions via Eqs. (11) and (12) represent their volumetric average over the micro-Raman collection volume.

The phonon frequency shifts of modes with E_2 and A_1 symmetry given by Eqs. (3) and (4) are related to the changes in atomic coordinates and the valence electron configuration in response to changes in stress, electric field, and temperature.[17] However, the A_1 (LO) optical phonon mode is a longitudinal phonon-plasmon (LPP) coupled mode whose frequency and lifetime vary strongly with the free electron concentration. To investigate whether changes in the free electron concentration with changing drain bias could affect the experimental results in this study, we modeled the aggregate A_1 (LO) lineshape with a similar integral expression as Eq. (13) but with the Lorentzian lineshape replaced by the LPP lineshape,

$$I_{A_1(LO)}(\omega) \sim \int A(\omega; n(\vec{r}))\ \mathrm{Im}\left[-\frac{1}{\varepsilon(\omega; n(\vec{r}))}\right] d^3\vec{r}, \tag{14}$$

where the functions A and ε depend on the local free electron concentration $n(\vec{r})$ through the plasmon frequency.[68] We found from the ATLAS/BLAZE model that increasing the drain bias from $V_{ds} = 0$ V to 40 V in the pinched OFF state with $V_{gs} = -5$ V slightly decreased the free electron concentration in the top $\approx$10 nm of the GaN buffer (near the 2DEG) while the remainder ($\approx 1.4\ \mu m$) had a free electron concentration of $<10^{15}\ cm^{-3}$, regardless of the drain bias. This change in drain bias led to a simulated shift in A_1 (LO) peak position $\Delta\omega_{A_1(LO)}$ of less than $0.01\ cm^{-1}$, which is negligible compared to the peak shifts we measured due to stress and vertical electric field shown in Fig. 4(a). While it is possible in other transistor systems for the free electron concentration to affect the optical phonon frequencies of phonon-plasmon coupled modes, we do not believe it to be a significant concern for GaN HEMTs nor to affect the results of this study.

VI. CONCLUSIONS

As compound semiconductor devices, such as GaN HEMTs, continue to mature for high performance transistor applications, micro-Raman spectroscopy will continue to increase in importance for assessing their reliability. In this work, we demonstrated the unique ability to measure the mechanical stress in the *c*-plane and electric field along the *c*-axis of the GaN buffer in GaN HEMTs in the presence of temperature rise up to $\approx$150 °C via micro-Raman spectroscopy. This is achieved by measuring the changes in the peak position of three optical phonon modes of wurtzite GaN and determining the stress, electric field, and temperature coefficients from first principles calculations (DFT) or measurements on a bulk GaN sample. We showed good quantitative agreement between our measured results and a 3D electro-thermo-mechanical model, which offers insights into the electrostatic behavior of the transistor due to the presence of impurities in the GaN buffer. As one of the few experimental techniques that can directly measure electric field components in transistors under bias, we anticipate that this application of micro-Raman spectroscopy will be highly utilized in future studies of thermal, mechanical, and electrical characterization of GaN HEMTs and other next-generation solid-state devices.

ACKNOWLEDGMENTS

The authors acknowledge funding support provided by the MIT/MTL GaN Energy Initiative and the Singapore-MIT Alliance for Research and Technology (SMART) LEES Program. This work was also partially supported by the Air Force Research Laboratory High-Reliability Electronics Virtual Center team. K. R. Bagnall also acknowledges that this research was conducted with Government support under and awarded by DoD, Air Force Office of Scientific Research, National Defense Science and Engineering Graduate (NDSEG) Fellowship, 32 CFR 168a. The authors would like to thank Professor Jing Kong of the Department of Electrical Engineering and Computer Science at MIT and the MIT Laser Biomedical Research Group for providing the experimental facilities and Professor Michael J. Uren of the University of Bristol, Bristol, UK, for helpful technical discussions. The authors would also like to thank Dr. Omair I. Saadat, formerly with the Department of Electrical Engineering and Computer Science at MIT, for the SIMS measurements.

APPENDIX: THE EFFECTS OF IMPURITIES ON THE ELECTROSTATICS OF THE BUFFER AND THE AVERAGE VERTICAL ELECTRIC FIELD

One critical issue in the ATLAS/BLAZE model that strongly affects the electric potential and electric field distributions in the GaN buffer is the species and concentration of impurities, traps, or deep-levels (both intentional dopants and unintentional defects) incorporated during the epitaxial growth of GaN on foreign substrates. The manufacturer of the DUT we tested indicates that the GaN buffer is intentionally doped with iron (Fe) because Fe acts as a deep-level acceptor 0.7 eV below the conduction band[59] and helps us to minimize short-channel effects[69] and improve the RF power amplifier efficiency.[61] Secondary ion mass spectroscopy (SIMS) measurements of a different GaN-on-SiC wafer by the same manufacturer also show the presence of carbon (C) at a concentration of $\sim 10^{17}$ cm^{-3}, silicon (Si) at $\sim 2 \times 10^{16}$ cm^{-3}, and oxygen (O) at $\sim 10^{17}$ cm^{-3}, all of which are approximately uniform with depth in the GaN buffer. Carbon unintentionally incorporated during the metal organic chemical vapor deposition (MOCVD) growth of GaN can act as a shallow donor (C_{Ga}) just below the conduction band or a deep acceptor (C_N) 0.9 eV above the valence band.[57] Although SIMS cannot distinguish between these two cases, the lower formation energy of C_N suggests that most of the measured C is C_N when the GaN film is grown in a nitrogen-rich environment as we expect for this DUT. Both Si (Si_{Ga}) and O (O_N) act as shallow donors just below the conduction band[70] and are also unintentionally incorporated when present since the GaN buffer is designed to be highly resistive. Although a variety of other defects, such as N and Ga vacancies and threading dislocations, are possibly present in the GaN buffer of the DUT, we focus here on the interaction of Fe, C, Si, and O because we believe that the basic electrostatic behavior of the buffer is controlled by these impurities through their effect on the Fermi level.

The Fermi level of GaN in the presence of deep acceptors (Fe and C_N) and shallow donors (Si and O) is determined by their relative ionized concentrations expressed in the charge neutrality statement[71]

$$p - n + N_D^+ - [Fe^-] - \left[C_N^-\right] = 0, \tag{A1}$$

where n and p are the electron and hole concentrations, $N_D^+ = \left[Si_{Ga}^+\right] + [O_N^+]$ is the total ionized shallow donor concentration, and $[Fe^-]$ and $[C_N^-]$ are the ionized Fe and C_N concentrations, respectively. A plot of the Fermi level dependence on the total shallow donor concentration N_D is shown in Fig. 10(a), which demonstrates the effect of changing N_D relative to [Fe] and $[C_N]$ while $[C_N]$ is fixed at 10^{17} cm^{-3} and [Fe] is 4×10^{16} cm^{-3} or 3×10^{18} cm^{-3}. When the total shallow donor concentration is less than the C_N concentration, i.e., $N_D < [C_N]$, the Fermi level is pinned in the lower half of the bandgap near the C_N acceptor energy level (regardless of the Fe concentration) resulting in highly resistive, p-type GaN. As soon as $[C_N] \le N_D < [C_N] + [Fe]$, the Fermi level moves abruptly to the upper half of the bandgap and is pinned near the Fe acceptor energy level, making the GaN highly resistive, n-type material. When $N_D \ge [C_N] + [Fe]$, the Fermi level approaches the conduction band, making the GaN conductive, n-type material. Thus, both C_N and Fe render the GaN semi-insulating by pinning the Fermi level away from the valence and conduction bands, compensating the unintentional shallow donors. This behavior is also shown by the energy band diagrams from the ATLAS/BLAZE model for $N_D = 7 \times 10^{16}$ cm^{-3} $< [C_N] = 1 \times 10^{17}$ cm^{-3} (highly resistive, p-type) and $N_D = 1.1 \times 10^{17}$ cm^{-3} $\ge [C_N] = 1 \times 10^{17}$ cm^{-3} (highly resistive, n-type) with a typical graded Fe doping concentration varying from [Fe] = 3.6×10^{16} cm^{-3} to 3×10^{18} cm^{-3} used for RF devices.[61]

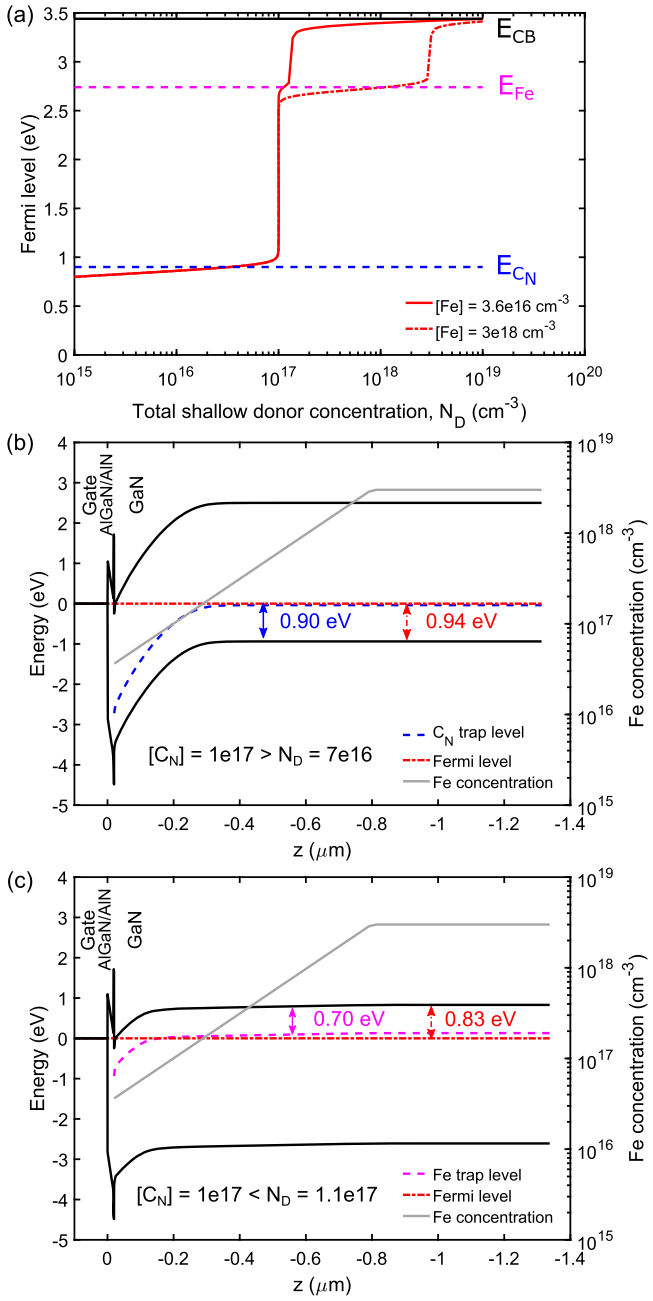

FIG. 10. (a) GaN Fermi level as a function of N_D calculated from charge neutrality with $[C_N]$ fixed at 10^{17} cm^{-3} for two different values of [Fe] and [(b) and (c)] equilibrium energy band diagram from the ATLAS/BLAZE model for $[C_N] = 10^{17}$ cm^{-3}, $N_D = 7 \times 10^{16}$ cm^{-3} and 1.1×10^{17} cm^{-3}, respectively, and a graded Fe doping profile from Ref. 61. Depending upon the relative values of $[C_N]$ and N_D, the Fermi level is pinned in either the lower half (b) or upper half (c) of the bandgap.

The location of the Fermi level in the bulk of the GaN buffer under zero bias determines the change in the electric potential distribution in the buffer as the drain bias changes, which we discuss briefly in Sec. IV A. If the Fermi level is pinned in the lower half of the bandgap, the buffer is a semi-insulating p-type material, and the buffer-drain and buffer-source junctions act as reverse biased p-n junctions. This means that the change in potential difference across the buffer in the drain access region and under the drain contact will be approximately equal to the drain bias until the buffer is fully depleted as shown in Fig. 5(a), after which there will be a lateral potential drop through the substrate from the drain to the source. This "floating p-type" buffer scenario has been linked to more prevalent charge trapping in intentionally C-doped GaN buffers for high voltage power conversion applications.[58] On the other hand, pinning the Fermi level in the upper half of the bandgap allows the drain and source to freely change the Fermi level in the bulk of the GaN buffer, resulting in a lateral potential drop from the drain to the source at any drain bias as shown in Fig. 5(b). There is still a vertical potential drop across the GaN buffer in the highly resistive n-type case due to the fact that the Fermi level crosses the Fe trap energy level at the top of the buffer, ionizing the Fe deep acceptors and creating a negative space charge region with a significant spatial variation along the gate-drain access region as seen in Fig. 5(b).

In a previous report aiming to investigate the effect of the Fe doping profile on the inverse piezoelectric strain in the GaN buffer measured by micro-Raman spectroscopy,[15] the authors found that the Raman peak shifts of a nominally undoped buffer were greater than those with intentional Fe doping and varied with the doping profile. We believe that the nominally undoped buffer satisfied the case of $[C_N] > N_D$, leading to p-type behavior and an average vertical electric field of $\bar{E}_z \approx -V_{ds}/L_b$ up to a drain bias of V_{ds} = 40 V. From this voltage and the thickness of the buffer, the authors correctly concluded that the net deep acceptor concentration $N_A - N_D$ was $\approx 3 \pm 0.5 \times 10^{16}$ cm^{-3}, where presumably $N_A \approx [C_N]$. However, the authors attributed the smaller Raman peak position changes of the intentionally Fe doped buffers with a higher peak vertical electric field over a more narrow depletion region because the Fe trap energy level was believed to also lie in the lower half of the bandgap at that time. This narrower depletion region of the buffer-drain p-n junction was believed to lead to a smaller depth-averaged IPE stress/strain measured by micro-Raman spectroscopy. As described in our recent review,[16] the depth-averaged values of the stress, strain, and electric field components must be related to one another; it is not theoretically sound to assert that the peak E_z component could be related to the depth-averaged ϵ_{zz} or σ_{xx} components under the assumption of a linear piezoelectric material in the continuum approximation.

From our ATLAS/BLAZE model and our discussion of the role of C_N and Fe controlling the position of the Fermi level of the bulk of the GaN buffer, we believe that the reason for lower peak shifts of the Fe doped samples is that these samples had highly resistive, n-type buffers. The resulting electric potential distribution had a strong lateral drop from the drain to the source and was highly dependent on where it was measured in the gate-drain access region via micro-Raman spectroscopy. Thus, the electric potential difference across the buffer and average vertical electric field was different for the nominally undoped and intentionally Fe doped samples, leading to a different magnitude of Raman peak position changes with drain bias.

[1] Y.-F. Wu, M. Moore, A. Saxler, T. Wisleder, and P. Parikh, in *Proceedings of the 64th Device Research Conference, State College, PA, USA 26 June-28 June 2006* (IEEE, 2006), pp. 151–152.
[2] E. Zanoni, M. Meneghini, A. Chini, D. Marcon, and G. Meneghesso, IEEE Trans. Electron Devices **60**, 3119 (2013).
[3] S. Chowdhury and U. K. Mishra, IEEE Trans. Electron Devices **60**, 3060 (2013).
[4] M. G. Ancona, S. C. Binari, and D. J. Meyer, J. Appl. Phys. **111**, 074504 (2012).
[5] S. Choi, E. Heller, D. Dorsey, R. Vetury, and S. Graham, J. Appl. Phys. **114**, 164501 (2013).
[6] P. Makaram, J. Joh, J. A. del Alamo, T. Palacios, and C. V. Thompson, Appl. Phys. Lett. **96**, 233509 (2010).
[7] F. Gao, S. C. Tan, J. A. del Alamo, C. V. Thompson, and T. Palacios, IEEE Trans. Electron Devices **61**, 437 (2014).
[8] M. Kuball, J. M. Hayes, M. J. Uren, T. Martin, J. C. H. Birbeck, R. S. Balmer, and B. T. Hughes, IEEE Electron Device Lett. **23**, 7 (2002).
[9] A. Sarua, H. Ji, M. Kuball, M. J. Uren, T. Martin, K. P. Hilton, and R. S. Balmer, IEEE Trans. Electron Devices **53**, 2438 (2006).
[10] M. Kuball and J. W. Pomeroy, IEEE Trans. Device Mater. Reliab. **16**, 667 (2016).
[11] A. Sarua, H. Ji, M. Kuball, M. J. Uren, T. Martin, K. J. Nash, K. P. Hilton, and R. S. Balmer, Appl. Phys. Lett. **88**, 103502 (2006).
[12] T. Beechem, A. Christensen, S. Graham, and D. Green, J. Appl. Phys. **103**, 124501 (2008).
[13] T. Batten, J. W. Pomeroy, M. J. Uren, T. Martin, and M. Kuball, J. Appl. Phys. **106**, 094509 (2009).
[14] S. Choi, E. R. Heller, D. Dorsey, R. Vetury, and S. Graham, IEEE Trans. Electron Devices **60**, 1898 (2013).
[15] A. Sarua, H. Ji, J. W. Pomeroy, M. J. Uren, T. Martin, and M. Kuball, Semicond. Sci. Technol. **25**, 085004 (2010).
[16] K. R. Bagnall and E. N. Wang, Rev. Sci. Instrum. **87**, 061501 (2016).
[17] K. R. Bagnall, C. E. Dreyer, D. Vanderbilt, and E. N. Wang, J. Appl. Phys. **120**, 155104 (2016).
[18] H. P. Sardesai and W. C. Nunnally, Rev. Sci. Instrum. **63**, 3918 (1992).
[19] B. Hajj, S. Perruchas, J. Lautru, G. Dantelle, T. Gacoin, J. Zyss, and D. Chauvat, Opt. Express **19**, 9000 (2011).
[20] C. Wetzel, T. Takeuchi, H. Amano, and I. Akasaki, J. Appl. Phys. **85**, 3786 (1999).
[21] F. Dolde, H. Fedder, M. W. Doherty, T. Nobauer, F. Rempp, G. Balasubramanian, T. Wolf, F. Reinhard, L. C. L. Hollenberg, F. Jelezko, and J. Wrachtrup, Nat. Phys. **7**, 459 (2011).
[22] M. Kuball, Surf. Interface Anal. **31**, 987 (2001).
[23] T. Beechem, S. Graham, S. P. Kearney, L. M. Phinney, and J. R. Serrano, Rev. Sci. Instrum. **78**, 061301 (2007).
[24] J. B. Cui, K. Amtmann, J. Ristein, and L. Ley, J. Appl. Phys. **83**, 7929 (1998).
[25] S. Choi, E. R. Heller, D. Dorsey, R. Vetury, and S. Graham, J. Appl. Phys. **113**, 093510 (2013).
[26] G. Callsen, J. S. Raparaz, M. R. Wagner, R. Kirste, C. Nenstiel, A. Hoffman, and M. R. Phillips, Appl. Phys. Lett. **98**, 061906 (2011).
[27] P. Giannozzi *et al.*, J. Phys.: Condens. Matter **21**, 395502 (2009).
[28] S. Baroni, S. de Gironcoli, A. Dal Corso, and P. Giannozzi, Rev. Mod. Phys. **73**, 515 (2001).
[29] C. Roder, S. Einfeldt, S. Figge, and D. Hommel, Phys. Rev. B **72**, 085218 (2005).
[30] P. Witczak, Z. Witczak, R. Jemielniak, M. Krysko, S. Krukowski, and M. Bockowski, Semicond. Sci. Technol. **30**, 035008 (2015).
[31] T. Ruf, J. Serrano, M. Cardona, P. Pavone, M. Pabst, M. Krisch, M. D'Astuto, T. Suski, I. Grzegory, and M. Leszczynski, Phys. Rev. Lett. **86**, 906 (2001).
[32] R. Resta, Rev. Mod. Phys. **66**, 899 (1994).
[33] E. A. Moore, K. R. Bagnall, E. N. Wang, and S. C. Badescu, "Corroborative determination of phonon deformation potentials in wurtzite GaN from Raman spectroscopy and first-principles modeling," (un published).
[34] A. R. Goni, H. Siegle, K. Syassen, C. Thomsen, and J.-M. Wagner, Phys. Rev. B **64**, 035205 (2001).

[35]R. S. Pengelly, S. M. wood, J. W. Milligan, S. T. Sheppard, and W. L. Pribble, IEEE Trans. Microwave Theory Tech. **60**, 1764 (2012).
[36]T. E. Beechem, Ph.D. thesis, Georgia Institute of Technology, 2008, pp. 62–64.
[37]Atlas User's Manual: Device Simulation Software, Version 5.22.1.R, Silvaco, Inc., Santa Clara, CA, 2015.
[38]Introduction to COMSOL Multiphysics, Version 5.2, COMSOL, Inc., Los Angeles, 2016.
[39]J. C. Freeman and W. Mueller, "Channel temperature determination for AlGaN/GaN HEMTs on SiC and sapphire," NASA Technical Report NASA/TM-2008-21544, December 2008.
[40]E. R. Heller, R. Vetury, and D. S. Green, IEEE Trans. Electron Devices **58**, 1091 (2011).
[41]B. E. Foutz, S. K. O'Leary, M. S. Shur, and L. F. Eastman, J. Appl. Phys. **85**, 7727 (1999).
[42]I. Vurgaftman and J. R. Meyer, J. Appl. Phys. **94**, 3675 (2003).
[43]M. Farahmand, C. Garetto, E. Bellotti, K. F. Brennan, M. Goano, E. Ghillino, G. Ghione, J. D. Albrecht, and P. Paul Ruden, IEEE Trans. Electron Devices **48**, 535 (2001).
[44]A. V. Sotnikov, H. Schmidt, M. Weihnacht, E. P. Smirnova, T. Y. Chemekova, and Y. N. Makarov, IEEE Trans. Ultrason., Ferroelectr., Freq. Control **57**, 808 (2010).
[45]L. Patrick and W. J. Choyke, Phys. Rev. B **2**, 2255 (1970).
[46]T.-H. Yu and K. F. Brennan, J. Appl. Phys. **91**, 3730 (2002).
[47]N. Maeda, K. Tsubaki, T. Saitoh, and N. Kobayashi, Appl. Phys. Lett. **79**, 1634 (2001).
[48]J. Cho, Y. Li, W. E. Hoke, D. H. Altman, M. Asheghi, and K. E. Goodson, Phys. Rev. B **89**, 115301 (2014).
[49]Silicon carbide substrates and epitaxy, Cree Inc., Durham, NC, 2011.
[50]E. A. Burgemeister, W. von Muench, and E. Pettenpaul, J. Appl. Phys. **50**, 5790 (1979).
[51]J. Cho, E. Bozorg-Grayeli, D. H. Altman, M. Asheghi, and K. E. Goodson, IEEE Electron Device Lett. **33**, 378 (2012).
[52]W. Liu and A. A. Balandin, J. Appl. Phys. **97**, 073710 (2005).
[53]J. P. Freedman, J. H. Leach, E. A. Preble, Z. Sitar, R. F. Davis, and J. A. Malen, Sci. Rep. **3**, 2963 (2015).
[54]Duralco 120: 500 °F electrically conductive adhesive, Cotronics Corp., Brooklyn, NY.
[55]O. Ambacher, J. Smart, J. R. Shealy, N. G. Weimann, K. Chu, M. Murphy, W. J. Schaff, L. F. Eastman, R. Dimitrov, L. Wittmer, M. Stutzmann, W. Rieger, and J. Hilsenbeck, J. Appl. Phys. **85**, 3222 (1999).
[56]N. Miura, T. Nanjo, M. Suita, T. Oishi, Y. Abe, T. Ozeki, H. Ishikawa, T. Egawa, and T. Jimbo, Solid-State Electron. **48**, 689 (2004).
[57]J. L. Lyons, A. Janotti, and C. G. Van de Walle, Appl. Phys. Lett. **97**, 152108 (2010).
[58]M. J. Uren, J. Moreke, and M. Kuball, IEEE Trans. Electron Devices **59**, 3327 (2012).
[59]M. Silvestri, M. J. Uren, and M. Kuball, Appl. Phys. Lett. **102**, 073501 (2013).
[60]S. M. Sze and K. K. Ng, *Physics of Semiconductor Devices*, 3rd ed. (John Wiley & Sons, Hoboken, 2007) pp. 79–84.
[61]M. J. Uren, D. G. Hayes, R. S. Balmer, D. J. Wallis, K. P. Hilton, J. O. Maclean, T. Martin, C. Roff, P. McGovern, J. Benedikt, and P. J. Tasker, in Proceedings of 1st European Microwave Integrated Circuits Conference, Manchester, UK, 2006.
[62]J. F. Nye, *Physical Properties of Crystals: Their Representation by Tensors and Matrices* (Oxford University Press, London, 1957), pp. 181–183.
[63]K. Kamitani, M. Grimsditch, J. C. Nipko, and C.-K. Loong, J. Appl. Phys. **82**, 3152 (1997).
[64]A. P. Mirogorodsky, M. B. Smirnov, E. Abelmounim, T. Merle, and P. E. Quintard, Phys. Rev. B **52**, 3993 (1995).
[65]G. Suriati, M. Mariatti, and A. Azizan, J. Mater. Sci.: Mater. Electron. **22**, 56 (2011).
[66]G. Pavlidis, S. Pavlidis, E. R. Heller, E. A. Moore, R. Vetury, and S. Graham, IEEE Trans. Electron Devices **64**, 78 (2017).
[67]T. Beechem, A. Christensen, D. S. Green, and S. Graham, J. Appl. Phys. **106**, 114509 (2009).
[68]T. Kozawa, T. Kachi, H. Kano, Y. Taga, M. Hashimoto, N. Koide, and K. Manabe, J. Appl. Phys. **75**, 1098 (1994).
[69]M. J. Uren, K. J. Nash, R. S. Balmer, T. Martin, E. Morvan, N. Caillas, S. L. Delage, D. Ducatteau, B. Grimbert, and J. C. De Jaeger, IEEE Trans. Electron Devices **53**, 395 (2006).
[70]R. Quay, *Gallium Nitride Electronics* (Springer-Verlag, Berlin, 2008), pp. 92–131.
[71]J. S. Blakemore, *Semiconductor Statistics* (Pergamon Press, New York, 1962), pp. 106–113.